THE GEOLOGICAL SOCIETY OF AMERICA®

Variability in Groundwater Flow and Chemistry in the Houzhai Karst Basin, Guizhou Province, China

JOSHUA M. BARNA[1,*]
ALAN E. FRYAR

Department of Earth and Environmental Sciences, University of Kentucky, 101 Slone Building, Lexington, KY 40506-0053

LE CAO

State Key Laboratory of Environmental Geochemistry, Institute of Geochemistry, Chinese Academy of Sciences, Guiyang, 550002, China

BENJAMIN J. CURRENS[2]

Department of Earth and Environmental Sciences, University of Kentucky, 101 Slone Building, Lexington, KY 40506-0053

TAO PENG

State Key Laboratory of Environmental Geochemistry, Institute of Geochemistry, Chinese Academy of Sciences, Guiyang, 550002, China

CHEN ZHU

Department of Earth and Atmospheric Sciences, Indiana University, 1001 E. Tenth Street, GY129, Bloomington, IN 47405-1405

Key Terms: ***Karst, Hydrogeology, Stable Isotope, Geochemistry, Dye Trace, China***

ABSTRACT

Understanding how karst aquifers store and transmit water and contaminants is an ongoing problem in hydrogeology. Multiple flow paths and recharge heterogeneity contribute to the complexity of these systems. This study explored karst-conduit connectivity and water-chemistry variability within the Houzhai catchment in Guizhou Province, China. Artificial tracer tests were conducted during both the monsoon and dry seasons to understand temporal variability in connectivity and water velocity between karst features. Multiple flow paths through the catchment were activated during the monsoon season and partially abandoned during the dry season. Additionally, gradient reversals during monsoonal high-flow events and as a result of pumping were observed. Synoptic water samples from several karst features taken during both monsoon and dry seasons elucidated spatial and temporal variability within the catchment. Water residence time was generally longer during the dry season, and flow within the Houzhai catchment was determined to be temporally dependent. Time-series sampling at the outlet spring following a monsoonal storm event captured chemical variability and identified multiple flow paths. Overall, this study refines widely applicable methods for studying karst systems to this catchment and provides a foundation for future studies in similar settings.

INTRODUCTION

Water movement through karst systems is complex and often not well understood, predominantly due to flow-path and recharge heterogeneity. This study explored groundwater flow by monitoring water parameters at multiple locations with varying temporal and spatial frequencies within the karstic Houzhai catchment. This 73.5 km^2 basin in Guizhou Province, China, is located in the center of the largest karst area in the world, the Southeast Asian karst region (Wang and Zhang, 2001; Li et al., 2010) (Figure 1). Exposed carbonate rocks account for just over 20 percent of the land surface in China, making this location a key area of karst research (Cao et al., 2015).

[1]Present address: ARM Group LLC, 9175 Guilford Road, Suite 310, Columbia, MD 21046
[2]Present address: Kentucky Division of Water, 300 Sower Boulevard, 3rd Floor, Frankfort, KY 40601
*Corresponding author email: jmba286@g.uky.edu

Figure 1. Context map of China with Guizhou Province in dark gray and the Houzhai catchment indicated by the circle.

Approximately 32,400 people lived within the Houzhai catchment as of 2010, and agriculture was the main livelihood for upwards of 95 percent of them (Li et al., 2010). Runoff from organic fertilizers within karst terrain has the potential to travel rapidly through the subsurface, carrying contaminants such as excess nutrients and fecal bacteria to springs, and thereby posing significant risk to drinking-water quality (Li et al., 2010). Another major threat to agriculture in this area is a thinning of the soil layer, known as rocky desertification, which is often exacerbated by a combination of climate change and deforestation (Liu et al., 2010). Soil loss not only reduces vegetation coverage and makes farming less productive, but it also decreases epikarst groundwater storage, thus making springs less reliable sources of water supply (Liu et al., 2010).

This study extended our understanding of the Houzhai catchment by using artificial tracers to identify primary flow paths and calculate groundwater velocities during both monsoon and dry seasons. It also examined spatial and temporal variations in water chemistry to draw inferences about system function. The study area was chosen because the karst-conduit network has been reasonably well delineated for at least two decades (Zhang et al., 1998). However, information regarding responses of springs in the catchment to storms is limited, and there are no known results of dye tracing within the catchment. This study provides insights into how this system may react to changes in environmental conditions such as land use/land cover and rainfall. Ideally, the results will contribute to knowledge needed for local policy makers to implement effective source-water protection practices.

BACKGROUND

Site Geology and Hydrology

The Houzhai catchment is classified as a typical mountain karst river basin (Wang and Zhang, 2001) (Figure 2). Elevation ranges from 1552 m above sea level (masl) in the headwaters to 1212 masl at the outlet, with slope decreasing from southeast to northwest (Zhang et al., 2017). Numerous karst peaks add to the relief, especially in the eastern part of the catchment. Geomorphically, the Houzhai catchment is characterized by cockpit karst, which is composed of conical hills and star-shaped valleys that formed during the Neogene under tropical climatic conditions (Yu and Zhang, 1988; Chen et al., 2018). Catchment topography transitions from peak-cluster depressions, characterized by closely spaced peaks and sinkholes that transfer runoff quickly underground, within the eastern, higher-elevation part of the catchment towards peak-cluster basin and hill combination topography (Figure 3), characterized by widely spaced peaks and springs located near the outlet of the catchment.

Karst features within the Houzhai catchment are developed in the Triassic Guanling Formation. Lithology consists mainly of limestone and dolomite, with beds dipping between 5° and 25° northwest (Liu et al., 2010). Carbonate rocks are usually exposed on the

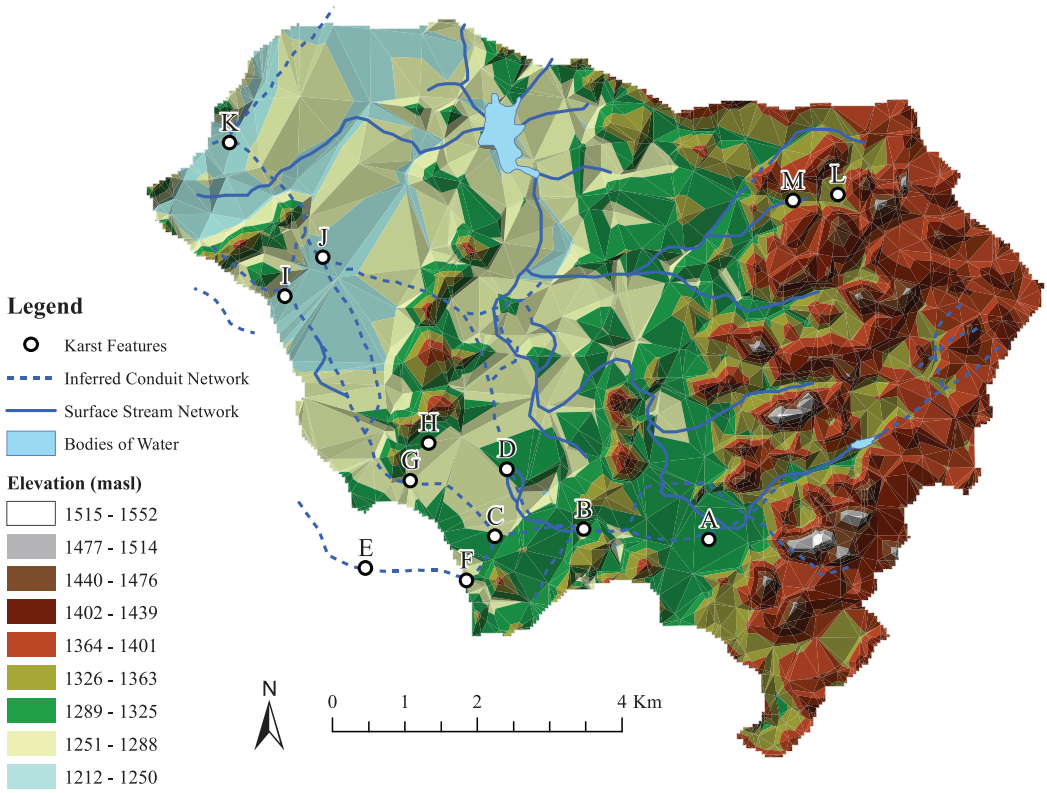

Figure 2. Houzhai catchment map with monitored karst features (letters refer to locations in Table 1), inferred karst conduit network, surface stream network, and bodies of water.

surface (Li et al., 2010). Soils are generally thin (average <50 cm) and discontinuous in the eastern half of the catchment and thicker in the western half (Li et al., 2010). These clayey soils have relatively low water-retention capacity overall (Yue et al., 2018). High clay content helps prevent water leakage from rice paddies.

Figure 3. Peak-cluster valley in Houzhai catchment between Sites C and D.

Due to the nature of karstic terrain, basin boundaries often cannot be well delineated and frequently overlap (White, 1988). Within the Houzhai catchment, shale and marlite units act as topographic boundaries to the north and southwest and provide a base for the karst aquifer (Chen et al., 2013). The Yuguan Fault acts as a no-flow boundary to the east and southeast (Chen et al., 2013). The Mugong River lies to the southwest, and Chen et al. (2013) stated that there is little exchange between the river and the karst conduit system. Water leaves the Houzhai catchment at Site K, in the northwest corner (Figure 2). Mean annual water temperature is 16.7°C (Yan et al., 2012). Surface water pH averages 7.5, fluctuating between 7.2 in the summer and 7.9 in the winter (Yan et al., 2012).

The Houzhai catchment has a subtropical humid climate, which is typical of southern China (Zhang et al., 2016). Around 80 percent of precipitation occurs during the monsoon season, which lasts from May to October (Li et al., 2010). Total annual precipitation in 2018 amounted to 1290 mm (basin annual average is ~1300 mm; Li et al., 2010). Climate change has impacted southwest China by increasing flood and drought frequency (Lian et al., 2015), which is likely to have adverse effects on agricultural productivity.

Water resources are used mainly for drinking and irrigation (Li et al., 2010). Corn and rice are the main crops grown in the wet season, while canola and various vegetables are grown in the dry season (Yue et al., 2018). "Cultivated area" accounts for approximately 20 percent of the total catchment area, two thirds of which consist of rice paddies (Hu et al., 2001). Both corn and rice are water-intensive to produce, and groundwater pumping from spring orifices for irrigation and domestic use was commonly observed in this study.

Previous Research

Significant efforts have been made to understand the karstic groundwater system of the Houzhai catchment. With regard to physical hydrology, Chen et al. (2018) conducted electrical resistivity tomography surveys to quantify the spatial heterogeneity of epikarst and aquifer permeability within the 1.25 km^2 Chenqi sub-catchment near the headwaters of the Houzhai basin. Hourly hydrometric and water isotope ($\delta^{18}O$ and $\delta^{2}H$) data were used to estimate storage and water age from fast-flow, hillslope, and slow-flow reservoirs in the Chenqi sub-catchment (Zhang et al., 2019). In the Houzhai catchment as a whole, Wang and Zhang (2001) documented the results of four "pulse tests," which are analogous to large-scale slug tests, between 1988 and 1991. Those authors found that water velocity ranged from 200 to 800 m/hr, with higher velocities during the wet season. These pulse tests were also used to identify three different "types of aquifer media" based on their response and flow recession curve (Yang, 2001). Zhang et al. (2016) found that karst-aquifer storage capacity increases along catchment flow paths, with more conduits and well-connected fissures upstream and more matrix and poorly connected fissures downstream. Li et al. (2010) reported that average annual discharges from underground and surface streams in the catchment are roughly equivalent, with 23.3×10^6 m^3/yr discharging from underground conduits and 24.9×10^6 m^3/yr discharging from surface streams. By comparison, using numerical simulations, Chen et al. (2013) found that surface streams only drain around 8 percent of total water discharge from the catchment during flooding periods, meaning that the bulk of flow occurs as groundwater discharge. Yue et al. (2018) found that water isotope values deviate from the global meteoric water line (GMWL) due to dry-season evaporative losses.

Previous hydrochemical studies focusing on the Houzhai catchment have included monitoring of dissolution rates and exchange between fast- and slow-flow systems during wet and dry periods (Zhang et al., 2017). In the Chenqi sub-catchment, Yang et al. (2012) found that soil CO_2 and rainfall play major roles in epikarst spring electrical conductivity (EC), partial pressure of carbon dioxide (P_{CO2}), and pH variability. Yan et al. (2012) conducted a long-term (21 year) study of surface-water chemistry at the Houzhai outlet and found that fluxes of dissolved Ca^{2+}, Mg^{2+}, HCO_3^-, and SO_4^{2-} slowly increased while Na^+, K^+, and Cl^- fluxes slowly decreased as a result of enhanced karst weathering. Those authors also found that rainfall had the most important influence on dissolved inorganic carbon (DIC) flux, an important parameter in constructing carbon budgets, which averaged 24.2 g C m^{-2} yr^{-1}. Using carbon stable-isotope ($\delta^{13}C_{DIC}$) compositions, Li et al. (2010) showed that the production of CO_2 from organic matter oxidation significantly impacts carbonate dissolution within the catchment. Diammonium phosphate, urea, and organic fertilizers are commonly applied to fields from April through July (Yue et al., 2018). Recent surveys by Buckerfield et al. (2019) showed that rural residents in the catchment were relatively unaware of the potential water-quality impacts associated with the usage of organic fertilizers.

Table 1. *Monitoring locations shown in Figure 2 (PKERS = Puding Karst Ecosystem Research Station [Barna, 2019]).*

Letter	Name	PKERS ID#
A	Xiao Shanba	98
B	Laoheitan	109
C	Daxing	121
D	Sanjianfang	123
E	Tian Guan	132
F	Aliangzhai	117
G	Liugu	129
H	Trash Spring	127
I	A Jiu Zhai	NA
J	Maokeng	302
K	Maoshuikeng	294
L	Hillslope Spring	167
M	Chenqi Outlet	171

METHODS

Synoptic Sampling

Summer synoptic samples were collected on June 16, 2018 at 11 locations throughout the southern portion of the Houzhai catchment (Sites A–K; Figure 2 and Table 1). Winter synoptic samples were collected on December 3, 2018 at the same locations, except Sites H and I, because they were dry. In addition to collecting samples for anion, metal(loid), and stable-isotope analyses, water parameters including temperature (T), specific conductance (SC; temperature-compensated EC), pH, and carbonate alkalinity were measured in the field. Water samples were filtered, acidified (for

Table 2. *Summary of summer and winter dye-tracing methods. Volumes of water for dissolving dye and flushing are approximate.*

Name	Summer Base Flow	Summer Storm Flow	Winter Base Flow	
Number of dye injections	1	1	2	
Date and time	6/17/18 13:30 hr	6/23/18 13:00 hr	12/5/18 10:35 hr	12/5/18 11:25 hr
Injection location	Site A	Site C	Site D	Site C
Dye type	Fluorescein	Eosine	Eosine	Sulforhodamine B
Dye amount (kg, solid)	5.5	3.2	1.8	1.8
Volume of water for dissolving dye (L)	300	175	100	100
Volume of flushing water (L)	80	80	50	50
Most recent precipitation event (days ago)	5	<1	19	19
Most recent precipitation event amount (mm)	19.2	60	1.2	1.2

preservation of metal[loid] samples), and refrigerated until analysis.

Dye Tracing and Storm-Flow Sampling

Passive samplers ("bugs") containing granular activated charcoal were deployed and then tested in order to identify the presence of fluorescent dyes in water samples. Before the summer and winter dye injections, background bugs were deployed to identify any pre-existing fluorescent dye within the system. During summer, one set of bugs was used to measure dye presence following the base-flow dye trace, and another set was used to identify storm-flow dye- trace presence. During winter, an effort was made to capture the first arrival of dye as it moved through the conduit network. To achieve this, bugs at each downgradient karst feature were swapped out daily or every other day. Charcoal from the bugs was analyzed using a scanning spectrofluorometer at the Kentucky Geological Survey (KGS) laboratory on the University of Kentucky campus, following Currens (2013).

At 1:30 pm on June 17, fluorescein dye powder dissolved in water was injected into the sinkhole at Site A and flushed with additional water (Table 2). Simultaneously, an ~900 kg aliquot of NaCl dissolved in ~4,000 L of water pumped from this sinkhole the previous day was also injected. The co-injection of saltwater with the dye solution likely induced mixing with groundwater in the underlying conduit because of density contrasts (Schincariol and Schwartz, 1990). The most recent precipitation event occurred on June 12 (total 19.2 mm), and there was no rain on the 17th, so this was considered a base-flow dye injection. In addition to charcoal bugs, water-level and EC loggers were deployed at Site B to measure any pressure or conductivity pulse from the salt injection (Barna, 2019).

At 1:00 pm on June 23, eosine dye powder dissolved in water was injected at Site C and flushed with additional water (Table 2). Approximately 60 mm of precipitation was recorded at Site B within 48 hours prior to injection. Unlike the base-flow dye trace at Site A, dye was no longer visible 50 minutes after injection. Sampling at Site K, the outlet spring of the Houzhai basin, began at 3:00 pm on the 23rd, continued every 2 hours for 24 hours, and then switched to hourly intervals for another 24 hours. In addition to collecting and filtering water samples for dye, alkalinity, anion, metal(loid), and stable-isotope analyses, water parameters including T, pH, and SC were also recorded from grab samples. EC and water-level loggers were deployed along the spring run ~370 m downstream of the orifice at Site K.

Two base-flow dye injections were conducted on December 5, 2018 (Table 2). At 10:35 am, eosine dye powder dissolved in water was injected at Site D and flushed with additional water, followed at 11:25 am by injection of sulforhodamine B powder dissolved in water and flushing with additional water at Site C. These dye injections began at base flow, with the last recorded precipitation event >0.2 mm/hr occurring 19 days prior (November 16). Because these injections were conducted during winter, water levels at both locations were significantly lower than those observed during summer.

Solute and Isotope Analyses

Anion, metal(loid), and $\delta^{13}C_{DIC}$ analyses were performed at the Institute of Geochemistry, Chinese Academy of Sciences, in Guiyang, China. Anions were measured using ion chromatography, while cations and SiO_2^0 were measured using inductively coupled plasma–optical emission spectrometry. Stable-isotope analyses for DIC were performed using a Thermo Fisher Scientific MAT 252 instrument. The $\delta^{13}C_{DIC}$ data are reported in per mil (‰) notation relative to Vienna Pee Dee Belemnite (VPDB). Water isotopes ($\delta^{18}O$ and $\delta^{2}H$) were measured at the Kentucky Stable Isotope Geochemistry Laboratory at the University of Kentucky by isotope-ratio infrared spectroscopy with a Los Gatos instrument. The data are reported in per

Table 3. *Ranges of summer and winter synoptic sample field parameters, analytes, and saturation indices with median values in parentheses.*

Field Parameter or Analyte	Summer	Winter
T (°C)	17.64–22.94 (18.45)	14.81–17.76 (17.26)
SC (μS/cm)	429–592 (492)	366–701 (578)
pH	6.77–8.10 (7.02)	6.72–7.36 (7.16)
Carbonate alkalinity (mg/L $CaCO_3$)	141–192 (183)	190–257 (209)
Ca^{2+} (mg/L)	61.09–93.93 (81.59)	59.92–117.89 (104.23)
K^+ (mg/L)	2.32–8.70 (3.51)	1.11–11.20 (4.79)
Mg^{2+} (mg/L)	10.67–19.20 (17.94)	22.91–28.17 (24.95)
Na^+ (mg/L)	1.87–6.08 (3.71)	1.97–35.01 (7.53)
SiO_2^0 (mg/L)	4.32–9.34 (5.27)	3.01–5.45 (5.05)
Sr^{2+} (mg/L)	0.98–2.30 (1.65)	0.27–3.82 (3.09)
Mg/Ca	0.21–0.45 (0.35)	0.35–0.69 (0.41)
$\delta^{13}C_{DIC}$ (‰ PDB)	−13.21 to −8.71 (−12.24)	−12.27 to −8.82 (−11.77)
δ^2H (‰ VSMOW)	−67.1 to −47.5 (−50.2)	−57.0 to −52.0 (−55.59)
$\delta^{18}O$ (‰ VSMOW)	−9.76 to −6.89 (−7.57)	−8.36 to −7.41 (−8.12)
F^- (mg/L)	0.18–0.34 (0.24)	0.19–0.78 (0.34)
Cl^- (mg/L)	6.30–12.82 (8.52)	4.79–57.34 (11.91)
NO_3^- (mg/L)	13.74–27.56 (24.68)	14.52–20.72 (16.67)
SO_4^{2-} (mg/L)	46.63–110.63 (64.26)	28.20–191.28 (136.88)
NO_2^- (mg/L)	0.03–0.53 (0.28)	<0.05
Br^- (mg/L)	<0.2	<0.2
$SI_{calcite}$	−0.53 to 0.78 (−0.24)	−0.377 to 0.11 (−0.11)
$SI_{dolomite}$	−1.62 to 1.24 (−0.92)	−1.15 to −0.14 (−0.56)
$SI_{strontianite}$	−1.85 to −0.46 (−1.45)	−1.95 to −0.85 (−1.30)
SI_{gypsum}	−1.88 to −1.46 (−1.74)	−2.18 to −1.19 (−1.36)
$SI_{celestite}$	−2.03 to −1.37 (−1.73)	−2.84 to −0.99 (−1.18)

mil notation relative to Vienna Standard Mean Ocean Water (VSMOW).

Solute data and additional parameters, including alkalinity, T, and pH, were entered into the geochemical modeling program PHREEQC (version 3.4.0 with phreeqc.dat database file; Parkhurst and Appelo, 2013) to calculate charge balances and saturation-index (SI) values. Eighty-five percent of the water samples charge-balanced to within 2 percent error, and the largest error was <5 percent. Phases of interest for SI calculations included calcite ($CaCO_3$), dolomite ($CaMg(CO_3)_2$), strontianite ($SrCO_3$), gypsum ($CaSO_4 \cdot 2H_2O$), and celestite ($SrSO_4$). Results of analyses and modeling calculations are tabulated in Barna (2019).

RESULTS

Synoptic Sampling

Physical and chemical water parameters fluctuated spatially and temporally throughout the Houzhai catchment. Ranges of summer and winter synoptic values for field parameters and analytes are listed in Table 3. Water T was, on average, 1.2°C cooler during winter than during summer. Specific conductance and alkalinity values were higher overall in the upper (southeast) part of the catchment and during the winter, whereas pH was also higher during the winter, but without a definitive spatial trend. The Na^+ and Cl^- concentrations at Site A (35.01 mg/L and 57.34 mg/L, respectively) were anomalously high during the winter. Mg/Ca ratios were generally higher during the winter (Table 3), especially at Sites J and K. Values of $\delta^{13}C_{DIC}$ tended to be higher during the winter, especially in the upper part of the catchment, whereas the opposite trend holds for δ^2H and $\delta^{18}O$ values. Maps detailing spatial variability in individual groundwater parameters measured during summer and winter synoptic sampling can be found in Barna (2019). Ca-HCO_3 was the dominant hydrochemical facies, which is typical of karst groundwater systems (Shuster and White, 1971; Liu et al., 2004).

Synoptic sample δ^2H and $\delta^{18}O$ values fell along the GMWL (Figure 4), with winter samples generally more depleted than summer samples. Nine of the summer samples clustered around average values of −50.8‰ for δ^2H and −7.63‰ for $\delta^{18}O$, but Site A was considerably more depleted ($\delta^2H = -67.1$‰, $\delta^{18}O = -9.76$‰), and Site H was somewhat more enriched ($\delta^2H = -47.5$‰, $\delta^{18}O = -6.89$‰). Winter synoptic samples clustered around average values of −56.0‰ for δ^2H and −8.17‰ for $\delta^{18}O$, with only Site D markedly enriched ($\delta^2H = -52.0$‰, $\delta^{18}O = -7.41$‰). Figure 4 includes a summary of isotopic data collected within the Chenqi sub-catchment by Chen et al. (2018)

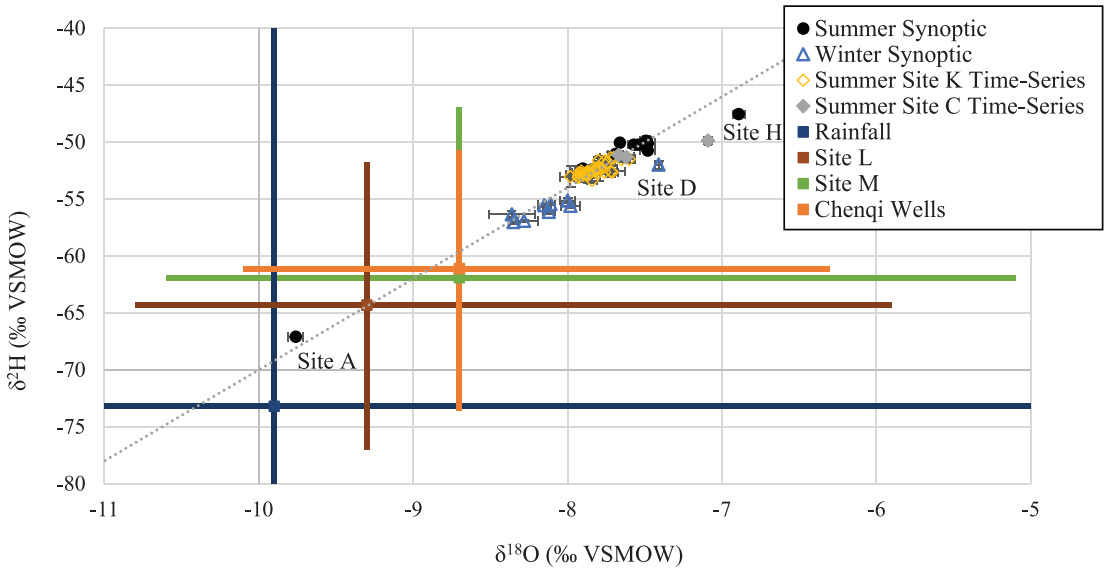

Figure 4. Plot of synoptic sample, time-series, and Chen et al. (2018) $\delta^{18}O$ versus $\delta^{2}H$ values relative to the global meteoric water line (dashed). Error bars represent one standard deviation; colored bars represent recorded data values. The isotopic range of the Chen et al. (2018) rainfall data ($\delta^{2}H = -120.2‰$ to $-17.9‰$, $\delta^{18}O = -16.4‰$ to $0‰$) was too large to be plotted.

for comparison with this study. These data show isotopic variability of wells, a hillslope spring (Site L), rainfall, and outlet discharge (Site M). Average isotopic values are depleted relative to the data in this study, except for Site A, with average rainfall values being most depleted.

Time-Series Analysis

The storm-flow trace at Site C occurred on June 23 at 1:00 pm, 3 hours after water level peaked at Site K (Figure 5). Therefore, the samples capture the falling limb of the storm event. Precipitation during this event, measured at the Site B weather station, occurred in two main pulses: 35.5 mm of rain peaking at 3:30 pm June 21, followed by 24.1 mm of rain peaking at 3:30 pm June 22 (Figure 5). A total of 6.5 mm of rainfall occurred after those two pulses, with only 2.0 mm during the sampling period at Site K. Minimum EC during the recession was logged at 9:35 am on June 24, nearly 24 hours after the stage peak (Figure 5), while pH reached a maximum at 11:00 am. Concentrations of several solutes (K^{+}, Na^{+}, SiO_2^{0}, Cl^{-}, Sr^{2+}, SO_4^{2-}) fell to minimum values 19–27 hours after the stage peak (Figure 6). Magnesium increased notably during the afternoon and evening of the 24th, and Mg/Ca values reached their maximum at 8:00 pm. Alkalinity generally trended upward (Barna, 2019), while NO_3^{-} generally decreased over the sampling interval (Figure 6C). There were no discernible trends for F^{-} or Ca^{2+} (Barna, 2019), nor for $\delta^{13}C_{DIC}$, which fluctuated within 0.8‰ (−11.55 to −12.34‰).

Values of $\delta^{2}H$ and $\delta^{18}O$ co-varied, increasing at the beginning of the sampling period and then sharply decreasing during the first half of June 24, followed by a saw-shaped pattern of fluctuations (Figure 6D). Site K $\delta^{2}H$ and $\delta^{18}O$ time-series sample values fell between winter and summer synoptic samples, with averages of $-52.4‰$ for $\delta^{2}H$ and $-7.82‰$ for $\delta^{18}O$ (Figure 4). Two of the three Site C time-series samples plotted within the summer synoptic sample cluster, but the first sample, which was taken immediately following the storm-flow dye trace, was significantly more enriched ($\delta^{2}H = -49.9‰$, $\delta^{18}O = -7.09‰$).

Dye Tracing

On June 18, 1 day after the base-flow dye injection at Site A, dye was visible in water discharging from all three of the observed outlets at Site B. Dye was still visible on June 19 at Site B and was visible at Site C on June 20, but dye was not visible at Site D or Site G. Except at Site K, none of the background bugs produced any positive dye spectra. The peak for fluorescein recorded by the Site K background bug was significantly lower than the peak observed from the bug that was deployed to capture the base-flow dye trace. Analyses of the charcoal bugs showed dye presence at Sites B, C, D, G, I, and K (Figure 7). The bug deployed at Site J was vandalized at an unknown time between deployment and retrieval, so even though enough

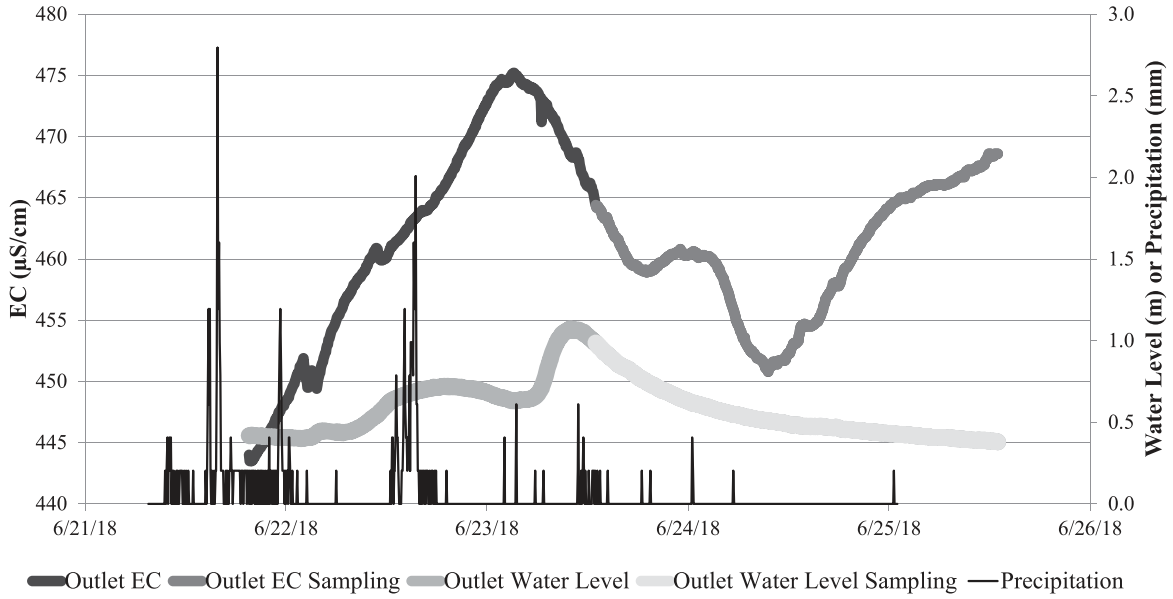

Figure 5. Plot showing continuously logged EC and water level at Site K leading up to and during the time of sampling in relation to precipitation data from the Site B weather station.

charcoal was recovered to test for dye, its absence does not conclusively indicate that no dye passed through Site J. The bugs at Sites E and F were lost prior to recovery and could not be tested.

Continuous loggers at Site B measured a water-level rise beginning ~40 minutes prior to the saltwater and dye injection (Figure 8). The water level initially crested 25 minutes before the injection and began to fall and then rebounded for ~2.5 hours before decreasing. Beginning ~17 hours after the ultimate water-level peak, a broad EC peak was superimposed on an increasing trend (Figure 8).

For the summer storm-flow trace, no dye was detected in the Site K water samples. However, all the bugs that were redeployed before the storm-flow trace indicated the presence of dye (Figure 9). The bug that was redeployed at Site F was positive for eosine. The bugs at Sites G and K were positive for both fluorescein and eosine, as was the bug that was deployed at Site I before the base-flow trace.

Before any of the winter dye injections, fluorescein still appeared to be visible at Site A when winter synoptic samples were taken (>5 months after injection). This result, which is consistent with elevated Na^+ and Cl^- values measured at the same time, could reflect slow leaching of co-injected dye and salt from soil around the sink. No dye was visible at Site B, and all the background bugs deployed tested negative for dye. One day after the winter base-flow injections, which occurred on December 5, dye was still visible but much less concentrated at the injection locations (Sites C and D). Three days after the injections, residual dye adsorbed to the soil and sediment substrate was observed at each injection site, but no dye was visible in the water. Pumping was observed during each visit to Site E but not at other sites. Site G was the only downgradient location where dye was visibly present in the water after injection. The first observation was 3 days after dye injection; the color became darker on day 4 and fainter on day 5. Based on this visible change, the main dye pulse arrived at Site G 4 days after injection.

One day after the injections, the bug deployed at Site F recorded the arrival of sulforhodamine B, the dye used at Site C (Figure 10). The following day, sulforhodamine B was detected in bugs from Sites E and F, and bugs confirmed the presence of dye at Site G 4 days after injection (Figure 10). In order to extend the monitoring time as long as possible, bugs were deployed at Sites J and K on December 10 and retrieved on December 13th. Sulforhodamine B was positively identified from the Site K bug, but no dye was observed at Site J at any point during the winter (Figure 10). Based on the bug results for sulforhodamine B, and assuming straight-line flow paths, winter base-flow velocities from Site C to several other karst features were estimated (Table 4).

DISCUSSION

Synoptic Sampling

Specific conductance and carbonate alkalinity can be seen as analogues for water residence time (Hess and White, 1988; Chen et al., 2018). These parameters

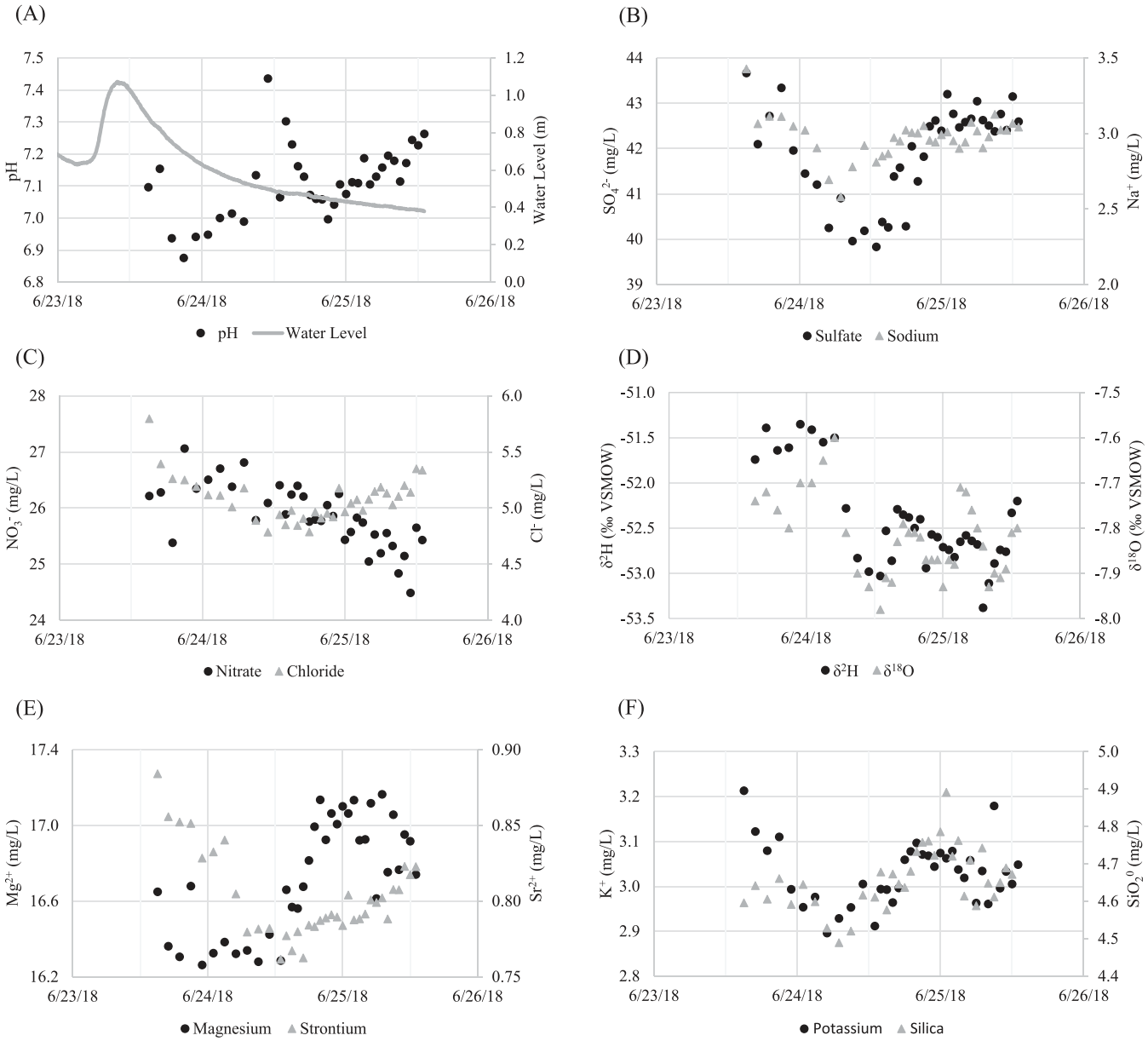

Figure 6. Plots showing pH and water level (A), sulfate and sodium (B), nitrate and chloride (C), δ^2H and $\delta^{18}O$ (D), magnesium and strontium (E), and potassium and silica (F) values during time-series sampling. Error for $\delta^2H = 0.3‰$. Error for $\delta^{18}O = 0.05‰$.

are generally higher during winter. This is likely because less water is flowing within the conduit system during the dry season, meaning that hydraulic heads and groundwater velocities are lower.

Residence time and lithology seem to be the two main controls on Mg/Ca ratios (Langmuir, 1971; Wigley, 1973; Plummer, 1977; Lohmann, 1988; and Fairchild et al., 1996). Longer residence times, either as a result of slower water velocity or longer flow paths, correspond with higher Mg/Ca ratios. This partly explains the increased Mg/Ca ratios in the winter and towards the outlet. Additionally, Sites J and K are located within the uppermost unit of the Guanling Formation, which is composed chiefly of dolomite. This lithologic variability likely accounts for some of the change in water chemistry. Similarly, higher SO_4^{2-} concentrations during winter may reflect a greater contribution of deep groundwater that has dissolved more gypsum along its flow path (Yan et al., 2012; Yang et al., 2012).

Site H seems to be an outlier compared to the other karst features. It was the only karst feature at which no dye was observed during the summer baseflow trace (Figure 7). Additionally, water parameter

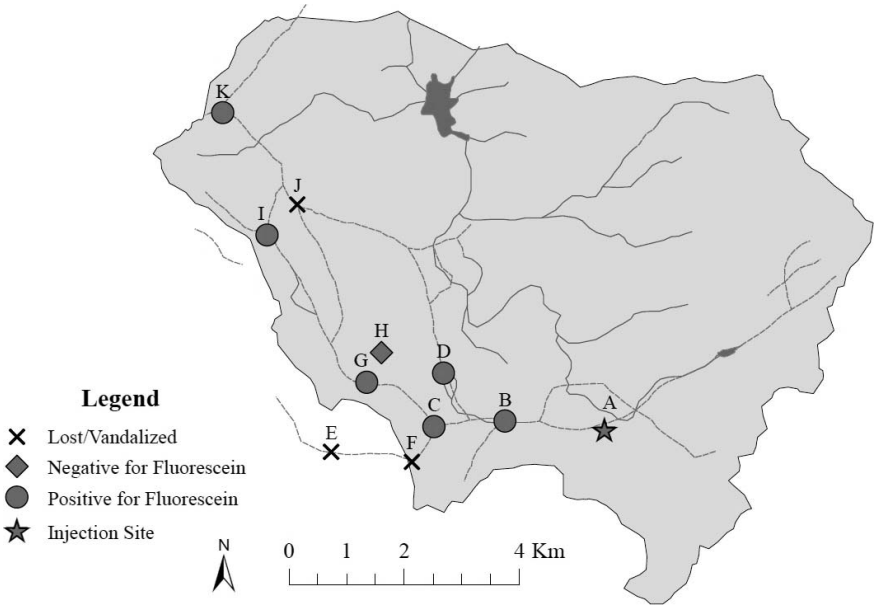

Figure 7. Map showing summer base-flow dye-trace bug results.

measurements such as SC, alkalinity, and Mg/Ca ratios were all notably lower than other springs. Water temperature was close to the diurnal range of temperatures logged at Site C (Barna, 2019). Overall, this suggests that flow-path lengths at Site H are relatively short and that it is perched above the main conduit network.

A comparison of $\delta^{13}C_{DIC}$ data from the synoptic samples shows a statistically significant ($p < 0.01$) increase in $\delta^{13}C_{DIC}$ from summer to winter (from −12.24 to −11.77‰ for median values; Table 3). The $\delta^{13}C_{DIC}$ values during the summer were roughly midway between C_3 plant $\delta^{13}C$ values (−28‰) and rock $\delta^{13}C$ values (0‰), and close to C_4 plant $\delta^{13}C$

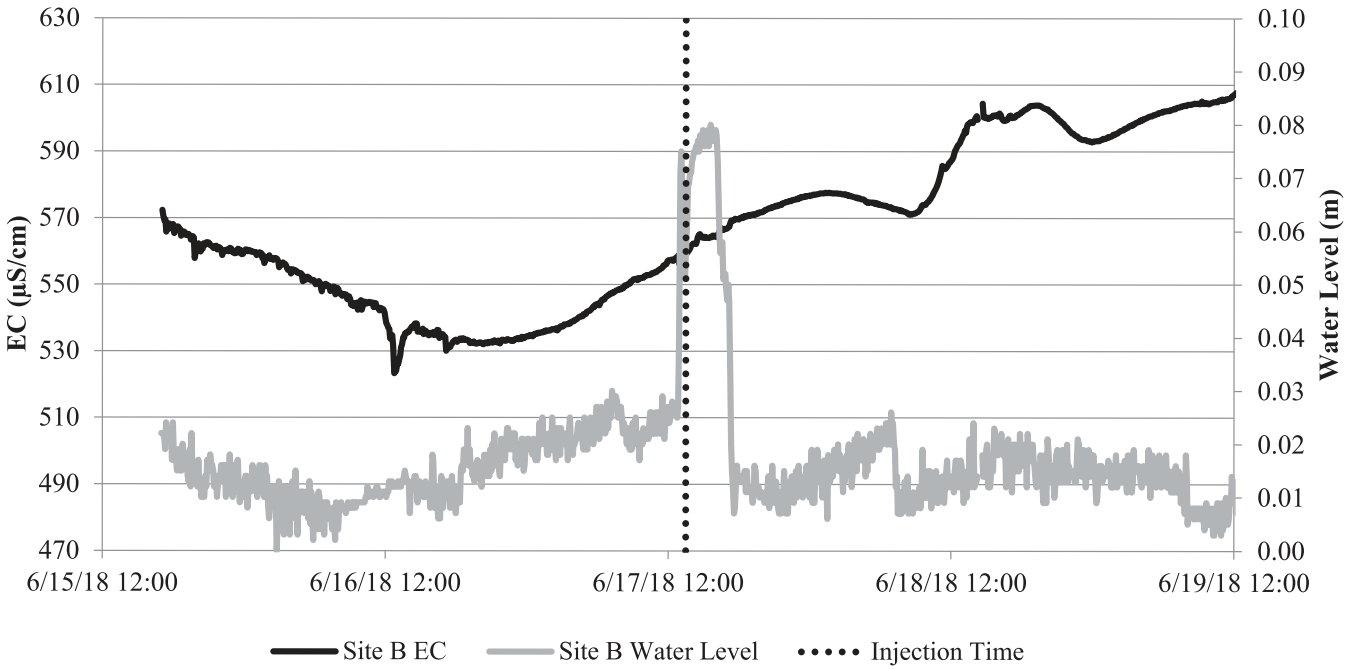

Figure 8. Plot showing water level (gray) and EC (black) at Site B, with the Site A injection time marked (vertical dotted line).

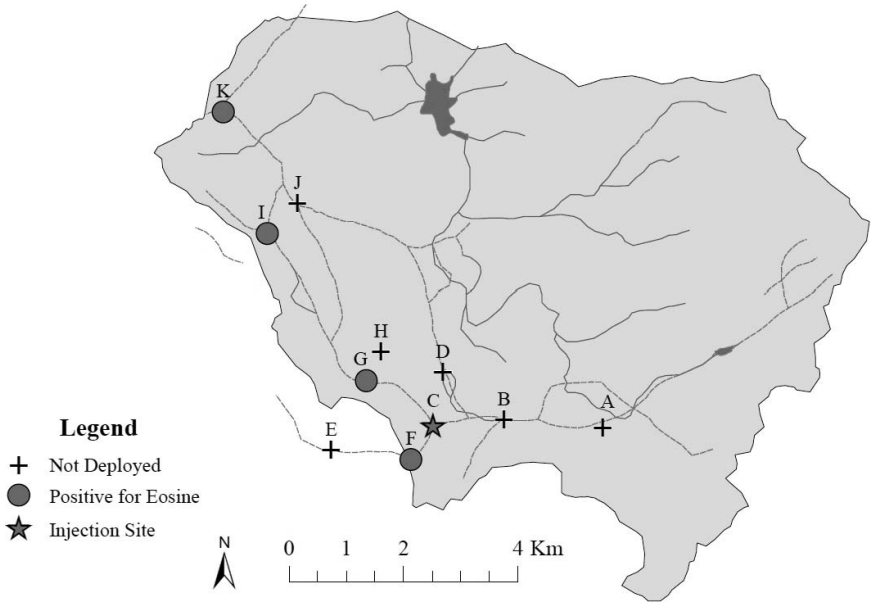

Figure 9. Map showing summer storm-flow dye-trace bug results.

values (−14‰) (O'Leary, 1988). Winter synoptic samples shifted closer towards the rock $\delta^{13}C$ end of the spectrum, as observed by Li et al. (2010). This is consistent with longer residence times, increased dissolution, and less oxidation of organic material during winter. While the main crop within the catchment is rice (a C_3 plant), corn (a C_4 plant) is also grown. Oxidation of other plant matter also likely influences $\delta^{13}C$ values. One notable outlier in the data is Site J, which showed a more enriched $\delta^{13}C_{DIC}$ value than the other locations in both summer and winter. The dissolution of more dolomite around Site J could explain this anomalous $\delta^{13}C$ value. Sheppard and Schwarcz (1970) found that dolomite $\delta^{13}C$ values are ∼1‰ higher than co-occurring low-Mg calcite. Site J showed the highest winter Mg/Ca ratio and third highest Mg/Ca ratio in the summer. Given that alkalinity values at Site J were not particularly high, isotopic variation as a result of lithologic variability, rather than the total amount of dissolution, is likely the cause of this enrichment.

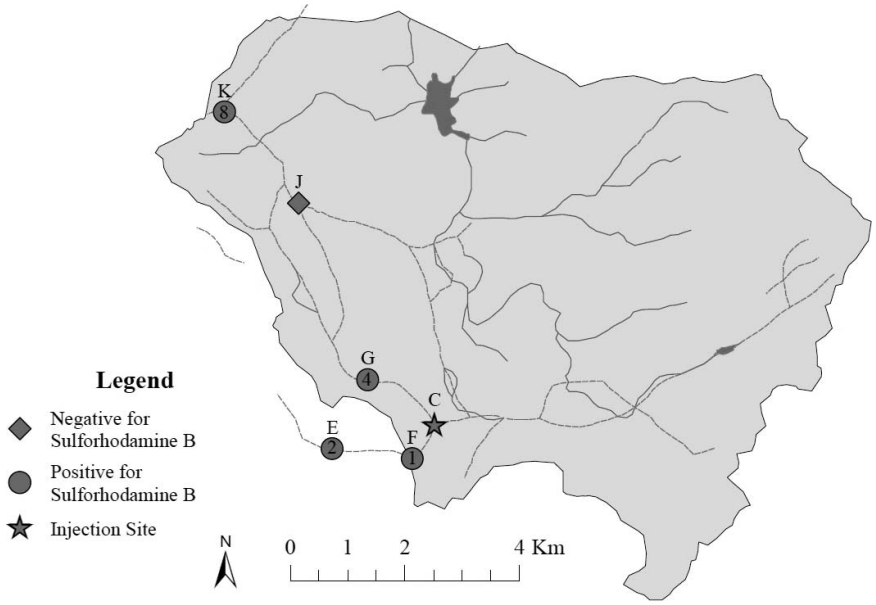

Figure 10. Winter base-flow dye-trace map with numbers representing the number of days after the trace that dye arrived at that karst feature.

Table 4. *Summary of inferred groundwater flow velocities under different hydrologic conditions.*

Velocity	Value (km/d)
Summer base flow	
Site A to Site B	2
Site A to Site K	≥2.6
Summer storm flow	
Site C to Site K	>3.7
Winter base flow	
Site C to Site F	>0.75
Site C to Site E	1–2
Site C to Site G	0.4–0.5
Site C to Site K	0.9–1.5
Site D to Site J	<0.6

The observation that water samples generally fell along the GMWL on a plot of δ^2H versus $\delta^{18}O$ suggests that evaporation was minimal at most locations. This is in contrast with the observations of Yue et al. (2018) and may reflect the fact that those authors sampled surface water, which is more prone to evaporation, as well as groundwater. The most depleted sample, from Site A during the summer, appears to have been a mixture of rainwater and groundwater, even though it had not rained for 5 days before sampling. The relatively low alkalinity and Cl^- concentration of the sample support the inference of groundwater dilution by rainwater, consistent with the inference that Site A is a sinkhole that subaerially exposes the water table. The two most enriched samples, from Sites H and C (at the time of injection), both fell below the GMWL, which suggests evaporation (Fritz et al., 1976; Lakey and Krothe, 1996). The anomalously enriched sample at Site C may have resulted from overflow of partly evaporated paddy water into the pool during the previous storm, which is consistent with observations during dye injection. The summer synoptic sample from Site K fell within the field of time-series storm samples from that spring and was more depleted than other summer synoptic samples (apart from Site A). This is consistent with Site K discharging a substantial component of deeper groundwater recharged at higher elevation within the basin. The relatively enriched values for the winter sample at Site D may indicate that the site is not well connected to the main conduit network during the dry season. The northern branch of the network may transmit water more slowly, which could explain why the eosine injected at Site D was not observed at any other karst feature. Except for Site A in summer, δ^2H and $\delta^{18}O$ values in this study were more enriched than average values of rainfall and groundwater samples collected from June to August 2017 in the higher-elevation Chenqi sub-catchment (Chen et al., 2018; Zhang et al., 2019) (Figure 4).

Based on geochemical modeling calculations, details of which are provided in Barna (2019), synoptic water samples were closer to saturation with respect to calcite during winter, especially in the southwestern-most part of the catchment. This was likely a result of less dilution and slower flow, allowing the water to approach equilibrium with the matrix, as well as retrograde solubility (Ford and Williams, 2007). Water samples were generally more undersaturated with respect to dolomite. Like calcite, $SI_{strontianite}$ winter values were somewhat closer to saturation than summer values. All water samples were undersaturated with respect to gypsum and celestite, and both indices were generally more negative during the summer, except at Sites J and K. Higher sulfate concentrations as a result of slower flow, especially in the upper catchment, can account for higher gypsum and celestite saturation indices during the winter. Overall, the geochemical analysis supports the inference of seasonal variability in groundwater velocity within the catchment.

Time-Series Analysis

The arrival of storm flow at Site K was indicated by minimum values of SC, pH, and concentrations of various solutes (Cl^-, SO_4^{2-}, Na^+, K^+, Mg^{2+}, Sr^{2+}, SiO_2^0) ~1 day after the stage peak (Figure 6). The fact that secondary minima and maxima followed the EC minimum and pH maximum suggests the arrival of a second storm pulse (Figures 5 and 6). The distinctive Mg^{2+} response could have resulted from spatial variability in carbonate lithology within the basin. The broad decline in NO_3^- concentration during the recession (Figure 6C) suggests a gradual flushing of fertilizer, which is liberally applied to rice paddies throughout the catchment.

More distinctly than solutes and field parameters, the δ^2H and $\delta^{18}O$ time-series plot for Site K appears to show three pulses of recharge, as indicated by successive drops and rebounds (Figure 6D). This may represent recharge from progressively farther up-gradient within the watershed, particularly since δ^2H is most depleted for the third pulse, consistent with higher-elevation recharge and with rainout (Darling et al., 2005). This is supported in comparison with the relatively depleted values measured within the Chenqi sub-catchment (Chen et al., 2018; Zhang et al., 2019) (Figure 4). Alternatively, the three pulses observed at Site K could represent contributions from different branches of the conduit network. The best way to test this hypothesis would be to conduct a tracer test, coupled with isotopic sampling, along each branch during a summer storm event.

The time-series SI plots for carbonate minerals (calcite, dolomite, and strontianite) have similar shapes

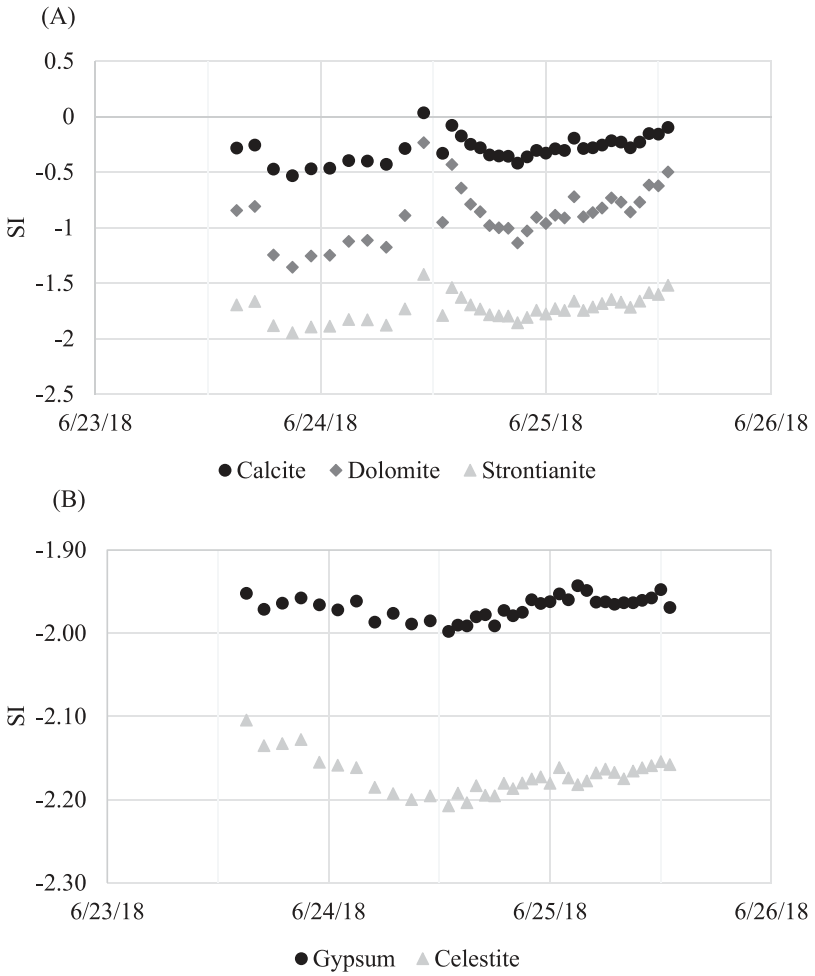

Figure 11. Saturation indices for carbonate minerals (A) and sulfate minerals (B).

(Figure 11A), which mirror pH time-series measurements. The SI plots of the sulfate minerals, gypsum and celestite (Figure 11B), both mirror the U-shaped SO_4^{2-} pattern. For carbonate minerals, maximum SI values occurred 4 hours after breakthrough of storm-water pulses, as indicated by local EC and T minima (Barna, 2019), and these maximum SI values were greater than values observed during synoptic (base-flow) sampling. For sulfate minerals, all SI values were less than those observed during synoptic sampling, and minimum values occurred 6 hours after breakthrough of storm-water pulses.

Dye Traces

Multiple conduit flow paths remained active at base flow during the monsoon season, as indicated by the presence of dye at both Sites C and D (Figure 12A). Both the Site B and Site C bugs produced eluent that had enough dye to be visible to the naked eye, consistent with visual observations in the field. The bug recovered from Site D during summer base flow also produced eluent with a visible amount of dye, although not as bright as Site B or Site C, which suggests that Site D is located on a secondary pathway. The negative dye result at Site H is consistent with other factors suggesting that this spring is a high-level overflow and is not continuously connected to the conduit system. The negative result at Site J may be due to vandalism of the bug before the arrival of the dye because, based on the inferred conduit flow paths, dye likely traveled via both conduit pathways (Figure 2).

The low-level detection of fluorescein in the background bug at Site K could be a false positive as a result of cross-contamination. However, neither the field blank nor any of the other background samples tested positive. It is more likely that the background detection is an artifact of fluorescein from a source such as radiator coolant, which is plausible given that the orifice is located beneath a highway bridge. The bug deployed to capture the base-flow dye trace at Site K showed a fluorescein peak approximately twice the intensity of

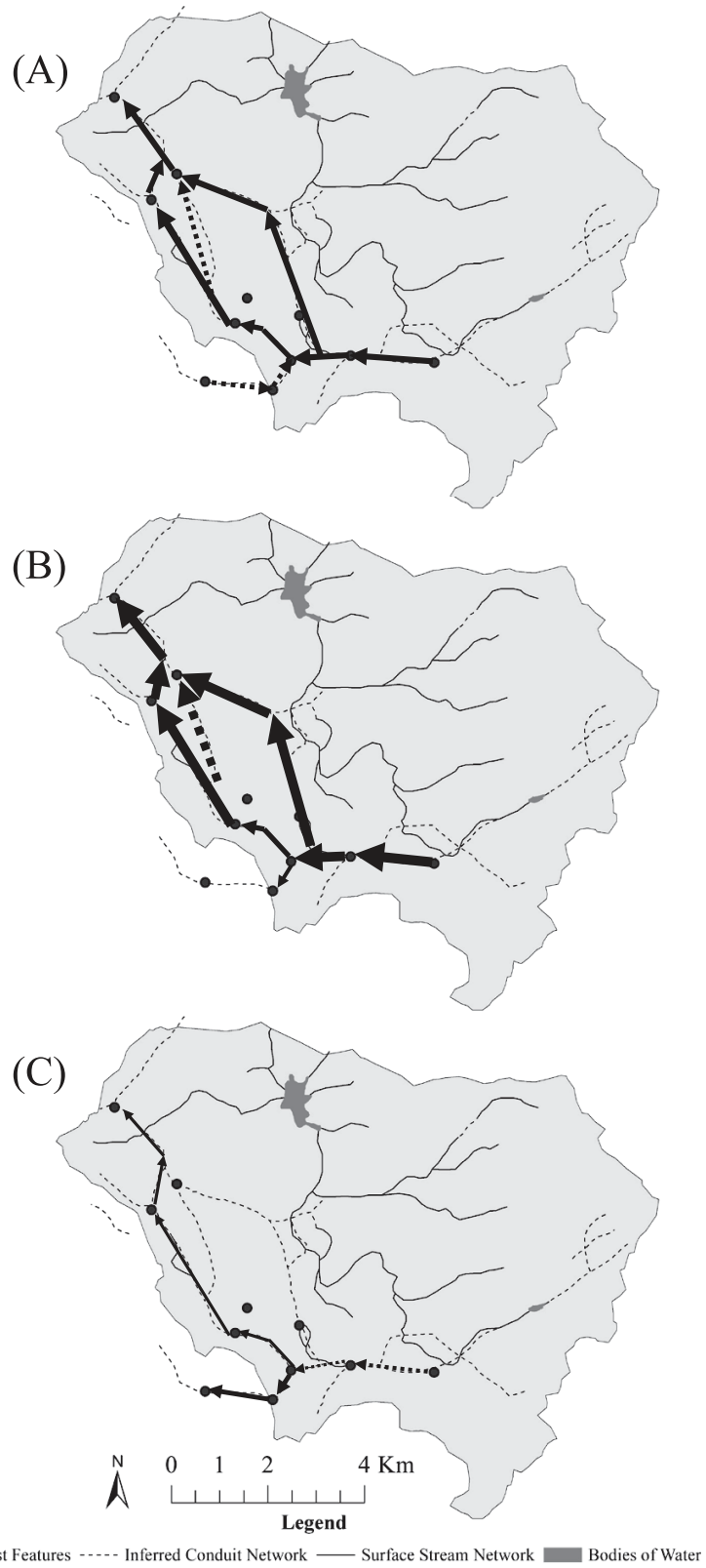

Figure 12. Conceptual maps showing summer base flow (A), summer storm flow (B), and winter base flow (C) through the Houzhai catchment. Thicker arrows correspond to faster groundwater velocities.

the background peak, which indicates the tracer velocity from Site A to Site K was ≥2.6 km/d (10.4 km in 4 days; Table 4).

The immediate water-level peak from the salt injection suggests a pressure pulse that moved through the system rapidly after the injection, displacing water already in the conduit system to discharge from the springs at Site B (Figure 8). The initial water-level rise beginning ~40 minutes before the injection may indicate a coincidental input of water, such as from one of the paddies around the sensor at Site B. The occurrence of a pressure pulse also suggests that the conduit system between Sites A and B experienced pipe-full conditions during the injection (Ryan and Meiman, 1996). Because water arriving at Site B during the pressure pulse was already moving through the system, there was no decrease in EC through dilution. The arrival of injected water was signaled by the EC peak ~21 hours later. Based on this arrival and an inferred conduit length of 1.75 km, the monsoon-season base-flow velocity between Site A and Site B was ~2 km/d (Table 4).

The bugs deployed at Sites G and K to monitor the storm-flow trace captured both fluorescein and eosine, suggesting that fluorescein had not been completely flushed from the system. The detection of both fluorescein and eosine for the bug at Site I, which was deployed from the start of the fluorescein trace until 48 hours after the eosine trace (a total of 8 days), suggests that this dry valley is connected to the trunk conduit network during high flow. Detection of eosine at Site F, which is inferred to be located on a tributary conduit flowing northeast to Site C, suggests a gradient reversal in this area during storm events (Figure 12B). The lower-bound distance on this gradient reversal is ~750 m.

An unexpected result of the winter dye traces was the relatively rapid flow from Site C towards Sites F and E (Figure 12C). Based on pre-existing maps of the conduit network, both karst features were thought to be up-gradient of Site C (Figure 2), especially during base-flow conditions. The reason for the inferred gradient reversal was likely the significant pumping observed at Site E. Because the rice paddies were dormant during this time, the water was likely used for other purposes, such as domestic use or construction. In general, inferred groundwater velocities were faster in summer than in winter, which is consistent with greater recharge and steeper hydraulic gradients during the wet season (Table 4).

There are several possible interpretations for the lack of dye observed at Site J. Groundwater velocity could have been <0.6 km/d (4.4 km over 8 days). Alternatively, Sites D and J may not be hydraulically connected during the dry season, but water from Site D would still be expected to discharge at Site K. Because Sites C and D are comparable in distance from Site K, the lack of detection of eosine (injected at Site D) and the detection of sulforhodamine B (injected at Site C) suggest slower velocities along the northern branch of the conduit network than the southern branch. The observation of sulforhodamine B at Site K but not at Site J suggests that Site J may not be located along the trunk conduit linking Sites G and K (Figure 12C). Sulforhodamine B may have flowed through a conduit located further west, possibly in connection with Site I. In general, karst conduit connectivity and groundwater velocity increase in response to precipitation (Shuster and White, 1971; Ryan and Meiman, 1996). Therefore, future changes in rainfall could increase flow variability between wet and dry seasons.

CONCLUSIONS

The Houzhai catchment in Guizhou Province, China, contains a complex karstic drainage network that shows variable behavior at both event (hours to days) and seasonal timescales. During summer, monsoon rains cause the conduit network to fill and overflow pathways to become active. During winter, overflow pathways remain dry, and some flow paths, such as the one that connects Site D to the rest of the conduit network, seem to decrease in velocity significantly or become hydrologically disconnected.

Carbonate dissolution is likely greater during the summer monsoon season due to the greater circulation of groundwater within the system. Saturation-index values, especially with respect to calcite, are generally more negative throughout the catchment during base-flow conditions in summer than in winter. This implies that flushing promotes mineral dissolution, as observed for DIC in surface water in the basin (Yan et al., 2012). Summer $\delta^{13}C_{DIC}$ samples are more depleted than winter samples, as observed by Li et al. (2010), indicating shorter residence times and increased oxidation of organic matter, especially from agricultural by-products such as rice leaves and corn stalks, during the summer. Summer storm events flush nitrate from the catchment; nitrate concentrations did not exceed either the Chinese standard of 20 mg/L NO_3-N (National Standards of the People's Republic of China, 1997) or the U.S. standard of 10 mg/L NO_3-N (U.S. Environmental Protection Agency, 2019). Organic fertilizer, possibly including human waste, is likely making its way into the karst conduit system. This and the relatively rapid groundwater velocities observed throughout the catchment pose significant contamination risks for local populations relying on groundwater for drinking water, given the findings of Buckerfield et al. (2019) regarding fecal pathogens.

This research builds on previous studies within the Houzhai catchment by constraining values of groundwater velocity during summer and winter baseflow conditions as well as during summer storm-flow events. Additionally, understanding of hydrologic connectivity within the southern portion of the Houzhai catchment has become more established. These collected data align well with preceding work completed at this site. Further application of dye-tracing techniques could significantly expand upon insights derived from this study. One potentially fruitful area of exploration could probe conduit connectivity and flow velocity during infrequent dry-season storm events. While likely more challenging to capture due to their relative rarity, comparing the results of that type of dye trace to those conducted in this study could significantly increase overall comprehension of groundwater flow variability. The heterogeneous nature of the Houzhai catchment conduit network likely generates responses to storm events that vary nonlinearly with fluctuations in the amount, intensity, and location of precipitation within the catchment, even within a single monsoon season.

The findings of this study have several practical implications for water-resource management in the catchment. Tracer tests provide estimates of travel times along the conduit network under various conditions, which are useful for understanding the susceptibility of water supplies to contamination and for parameterizing groundwater flow models (Chen et al., 2013; Zhang et al., 2017, 2019). In addition, the observed gradient reversal at Sites E and F in December indicates the potential for changes in flow rates and directions as a result of pumping. Consequently, there may be localized dewatering of conduits during the dry season. Overall, the combination of tracer injection with water-quality monitoring during base flow (synoptically and seasonally) and storm flow provides a foundation for further research on conduit connectivity and groundwater velocity.

ACKNOWLEDGMENTS

Thanks go to Andrea Erhardt and Junfeng Zhu for helping to shape the direction of this project. Laboratory assistance was provided by Jordan Munizzi, Andrea Conner, and Zhikang Wang. The field support of Driver Song, Guanru Zhang, Qianyun Cheng, Sarah Buckerfield, Qiangshan Gao, Xuemei Liu, and Yang Changan was invaluable. Funding for this project was provided through the University of Kentucky Ferm and Brown McFarlan funds, the University of Kentucky Confucius Institute, and the Chinese Academy of Sciences through the Opening Fund of the State Key Laboratory of Environmental Geochemistry (SKLEG2016903). Three anonymous reviewers provided thoughtful comments that improved the manuscript.

REFERENCES

Barna, J. M., 2019, *Variability in Groundwater Flow and Chemistry in the Houzhai Karst Basin, Guizhou Province, China*: Unpublished M.S. Thesis, Department of Earth & Environmental Sciences, University of Kentucky, Lexington, KY. Electronic document, available at https://doi.org/10.13023/etd.2019.109.

Buckerfield, S. J.; Waldron, S.; Quilliam, R. S.; Naylor, L. A.; Li, S.; and Oliver, D. M., 2019, How can we improve understanding of faecal indicator dynamics in karst systems under changing climatic, population, and land use stressors?—Research opportunities in SW China: *Science Total Environment*, Vol. 646, pp. 438–447.

Cao, J.; Yuan, D.; Tong, L.; Mallik, A.; Yang, H.; and Huang, F., 2015, An overview of karst ecosystem in southwest China: Current state and future management: *Journal Resources Ecology*, Vol. 6, No. 4, pp. 247–256.

Chen, X.; Zhang, Y. F.; Zhou, Y. Y.; and Zhang, Z. C., 2013, Analysis of hydrogeological parameters and numerical modeling groundwater in a karst watershed, southwest China: *Carbonates Evaporites*, Vol. 28, No. 1–2, pp. 89–94.

Chen, X.; Zhang, Z.; Soulsby, C.; Cheng, Q.; Binley, A.; Jiang, R.; and Tao, M., 2018, Characterizing the heterogeneity of karst critical zone and its hydrological function: An integrated approach: *Hydrological Processes*, Vol. 32, pp. 2932–2946.

Currens, J. C., 2013, *Kentucky Geological Survey Procedures for Groundwater Tracing Using Fluorescent Dyes*: Kentucky Geological Survey, Series XII, Information Circular 26. Electronic document, available at https://kgs.uky.edu/kgsweb/olops/pub/kgs/IC26_12.pdf

Darling, W. G.; Bath, A. H.; Gibson, J. J.; and Rozanski, K., 2005, Isotopes in water. In Leng, M. J. (Editor), *Isotopes in Palaeoenvironmental Research*: Springer, Dordricht, The Netherlands, pp. 1–66.

Fairchild, I. J.; Tooth, A. F.; Huang, Y.; Borsato, A.; Frisia, S.; and McDermott, F., 1996, Spatial and temporal variations in water and stalactite chemistry in currently active caves: A precursor to interpretations of past climate. In Botrell, S. (Editor), *Proceedings of the Fourth International Symposium on the Geochemistry of the Earth's Surface*: University of Leeds, Ilkley, U.K., pp. 229–233.

Ford, D. C. and Williams, P. W., 2007, *Karst Hydrogeology and Geomorphology*: John Wiley & Sons, Chichester, U.K.

Fritz, P.; Cherry, J. A.; Sklash, M.; and Weyer, K. U., 1976, Storm runoff analysis using environmental isotopes and major ions. In *Interpretation of Environmental Isotope and Hydrochemical Data in Groundwater Hydrology*: International Atomic Energy Agency, Vienna, Austria, pp. 111–130.

Hess, J. W. and White, W. B., 1988, Storm response of the karstic carbonate aquifer of southcentral Kentucky: *Journal Hydrology*, Vol. 99, pp. 235–252.

Hu, X. J.; Chen, B.; Hu, X. H.; and He, G. H., 2001, Study on the model of rational land use in the karst areas of the Houzhai River Basin: *Carsologica Sinica*, Vol. 20, pp. 305–309.

Lakey, B. and Krothe, N. C., 1996, Stable isotopic variation of storm discharge from a perennial karst spring, Indiana: *Water Resources Research*, Vol. 32, No. 3, pp. 721–731.

Langmuir, D., 1971, The geochemistry of some carbonate ground waters in central Pennsylvania: *Geochimica Cosmochimica Acta*, Vol. 35, pp. 1023–1045.

Li, S.-L.; Liu, C.-Q.; Li, J.; Lang, Y.-C.; Ding, H.; and Li, L. B., 2010, Geochemistry of dissolved inorganic carbon and carbonate weathering in a small typical karstic catchment of southwest China: Isotopic and chemical constraints: *Chemical Geology*, Vol. 277, No. 3–4, pp. 301–309.

Lian, Y.; You, G.; Lin, K.; Jiang, Z.; Zhang, C.; and Qin, X., 2015, Characteristics of climate change in southwest China karst region and their potential environmental impacts: *Environmental Earth Sciences*, Vol. 74, pp. 937–944.

Liu, L. H.; Shu, L. C.; Chen, X. H.; and Oromo, T., 2010, The hydrologic function and behavior of the Houzhai underground river basin, Guizhou Province, southwestern China: *Hydrogeology Journal*, Vol. 18, No. 2, pp. 509–518.

Liu, Z. H.; Groves, C.; Yuan, D. X.; Meiman, J.; Jiang, G. H.; He, S. Y.; and Li, Q. A., 2004, Hydrochemical variations during flood pulses in the south-west China peak cluster karst: Impacts of $CaCO_3$-H_2O-CO_2 interactions: *Hydrological Processes*, Vol. 18, No. 13, pp. 2423–2437.

Lohmann, K. C., 1988, Geochemical patterns of meteoric diagenetic systems and their application to studies of paleokarst. In James, N.P., Choquette, P.W. (Editors), *Paleokarst*: Springer-Verlag, New York, pp. 58–80.

National Standards of the People's Republic of China, 1997, *Environmental Quality Standards for Surface Water*: Electronic document, available at http://english.mee.gov.cn/SOE/soechina1997/water/standard.htm

O'Leary, M. H., 1988, Carbon isotopes in photosynthesis: *Bioscience*, Vol. 38, No. 5, pp. 328–336.

Parkhurst, D. L. and Appelo, C. A. J., 2013, *Description of Input and Examples for PHREEQC Version 3: A Computer Program for Speciation, Batch-Reaction, One-Dimensional Transport, and Inverse Geochemical Calculations*: U.S. Geological Survey Techniques and Methods 6-A43.

Plummer, L. N., 1977, Defining reactions and mass transfer in part of the Floridan Aquifer: *Water Resources Research*, Vol. 13, pp. 801–812.

Ryan, M. and Meiman, J., 1996, An examination of short-term variations in water quality at a karst spring in Kentucky: *Groundwater*, Vol. 34, No. 1, pp. 23–30.

Schincariol, R. A. and Schwartz, F. W., 1990, An experimental investigation of variable density flow and mixing in porous media: *Water Resources Research*, Vol. 26, No. 10, pp. 2317–2329.

Sheppard, S. M. and Schwarcz, H. P., 1970, Fractionation of carbon and oxygen isotopes and magnesium between coexisting calcite and dolomite: *Contributions Mineralogy Petrology*, Vol. 26, pp. 161–198.

Shuster, E. and White, W. B., 1971, Seasonal fluctuations in the chemistry of limestone springs: A possible means for characterizing carbonate aquifers: *Journal Hydrology*, Vol. 14, pp. 93–128.

U.S. Environmental Protection Agency, 2019, *National Primary Drinking Water Regulations*: Electronic document, available at https://www.epa.gov/ground-water-and-drinking-water/national-primary-drinking-water-regulations

Wang, L. C. and Zhang, Y. Z., 2001, Karst conduit flow and its hydrodynamic characteristics—Houzhai River drainage basin in Puding, Guizhou, China, as an example: *Chinese Science Bulletin*, Vol. 46, pp. 45–51.

White, W. B., 1988, *Geomorphology and Hydrology of Karst Terrains*: Oxford University Press, New York.

Wigley, T. M. L., 1973, The incongruent solution of dolomite: *Geochimica Cosmochimica Acta*, Vol. 37, pp. 1397–1402.

Yan, J. H.; Li, J. M.; Ye, Q.; and Li, K., 2012, Concentrations and exports of solutes from surface runoff in Houzhai Karst Basin, southwest China: *Chemical Geology*, Vol. 304, pp. 1–9.

Yang, R.; Liu, Z. H.; Zeng, C.; and Zhao, M., 2012, Response of epikarst hydrochemical changes to soil CO_2 and weather conditions at Chenqi, Puding, SW China: *Journal Hydrology*, Vol. 468, pp. 151–158.

Yang, Y., 2001, A study of the structure of karst aquifer medium and the groundwater flow in Houzhai underground river basin: *Carsologica Sinica*, Vol. 20, No. 1, pp. 17–20.

Yu, J., and Zhang, H., 1988, Karst geomorphology in Puding, Guizhou Province: *Carsologica Sinica*, Vol. 7, No. 2, pp. 163–172.

Yue, F.-J.; Li, S.-L.; Zhong, J.; and Liu, J., 2018, Evaluation of factors driving seasonal nitrate variations in surface and underground systems of a karst catchment: *Vadose Zone Journal*, Vol. 17, 170071.

Zhang, R. R.; Shu, L. C.; Zhu, J. T.; Yu, Z. B.; and Jiang, P., 2016, Storage and drainage characteristics of a highly heterogeneous karst aquifer in Houzhai basin: *Groundwater*, Vol. 54, No. 6, pp. 878–887.

Zhang, Z.; Chen, X.; Cheng, Q.; and Soulsby, C., 2019, Storage dynamics, hydrological connectivity and flux ages in a karst catchment: Conceptual modelling using stable isotopes: *Hydrology Earth System Sciences*, Vol. 23, pp. 51–71.

Zhang, Z.; Chen, X.; and Soulsby, C., 2017, Catchment-scale conceptual modelling of water and solute transport in the dual flow system of the karst critical zone: *Hydrological Processes*, Vol. 31, No. 19, pp. 3421–3436.

Zhang, Z.; Zhang, J.; Yang, J.; and Shen, P., 1998, Research on the spatial structure of karst massif—Taking the basin of the Houzhai subterranean stream in Puding County for example: *Chinese Geographical Science*, Vol. 8, No. 3, pp. 256–263.